

Constraining the neutral hydrogen fraction during reionization: Cross-simulation inference using power spectrum and bispectrum

Anoop Krishna,^{1*} Deepthi Moorkanat,¹ Hiten,¹ Rajesh Mondal¹

¹*Department of Physics, National Institute of Technology Calicut, Calicut 673601, Kerala, India*

Accepted XXX. Received YYY; in original form ZZZ

ABSTRACT

The redshifted 21-cm signal is a unique probe of the early universe, particularly the Epoch of Reionization (EoR). While the 21-cm power spectrum has been the primary statistic for parameter inference, it fails to capture the non-Gaussian information in the signal, motivating the use of higher-order statistics such as the bispectrum. We perform a rigorous cross-simulation validation to infer the mean neutral hydrogen fraction (\bar{x}_{HI}) by training a Bayesian neural network on 21cmFAST simulations and applying it to mock observations generated by ReionYuga code. Our analysis spans six redshifts and includes realistic SKA system noise and cosmic variance, calculated from 50 statistically independent realizations. We find that the bispectrum adds useful information, but the improvement is moderate, with constraints tightened by $\sim 1.4\times$ the power-spectrum only case. The cross-simulation analysis also identifies a persistent systematic discrepancy between inferred and true values that often exceeds the statistical uncertainties, implying that modeling uncertainty remains the dominant limitation. Our results, therefore, indicate that the highly stringent constraints obtained in same-code validation studies may be overly optimistic, and mitigating cross-model systematics is crucial for robust parameter inference in the SKA era.

Key words: methods: statistical–cosmology; theory–dark ages, reionization, first stars–diffuse radiation

1 INTRODUCTION

The Epoch of Reionization (EoR) marks a crucial phase transition in cosmic history, occurring roughly between redshifts $z \sim 6 - 15$ (Becker et al. 2001; Planck Collaboration et al. 2020). During this period, the first luminous sources gradually heated and ionized the neutral hydrogen (H I) in the intergalactic medium (IGM) (Furlanetto et al. 2006; Pritchard & Loeb 2012). Probing this era directly remains one of the most ambitious goals in modern cosmology. The redshifted 21-cm emission from the hyperfine transition of H I provides a direct probe of the reionization process in three dimensions (Furlanetto et al. 2006; Morales & Wyithe 2010). With the advent of next-generation radio interferometers such as the Square Kilometre Array (SKA), and ongoing efforts from pathfinders including the Low-Frequency Array (LOFAR), the Murchison Widefield Array (MWA), and the Hydrogen Epoch of Reionization Array (HERA), we are entering an era where statistical characterization of the EoR 21-cm signal is becoming a reality (Tingay et al. 2013; DeBoer et al. 2017; van Haarlem et al. 2013).

The primary statistical measure for analyzing the 21-cm signal has been the power spectrum $P(k)$. The $P(k)$ captures the variance of brightness temperature fluctuations across different spatial scales. However, it is fundamentally limited when dealing with non-Gaussian fields (Bharadwaj & Ali 2004; Mondal et al. 2017). The EoR 21-cm signal is highly non-Gaussian (Bharadwaj & Pandey 2005; Mondal et al. 2015) due to the underlying non-linearities in

the matter field and the complex, inhomogeneous nature of the reionization process. As ionized bubbles form around sources and grow until they eventually percolate (Iliev et al. 2006), they introduce complex phase correlations that the power spectrum, being second-order statistics, cannot resolve. Higher-order statistics, starting with the bispectrum, are therefore needed to fully describe the reionization process and break degeneracies between different physical drivers (Majumdar et al. 2018; Watkinson et al. 2017; Mondal et al. 2020).

The current challenge is to constrain the parameters that provide information regarding the underlying IGM and astrophysics. This approach typically involves Bayesian inference, often implemented via Markov Chain Monte Carlo (MCMC) sampling. Such inference is now computationally feasible due to semi-numerical simulation tools such as ReionYuga (Mondal et al. 2017) and 21cmFAST (Mesinger et al. 2011), as well as other variants, often coupled with neural network emulators for rapid likelihood evaluation.

Recent work by Tiwari et al. (2022) demonstrated that including the bispectrum in parameter inference significantly enhances the constraints on EoR parameters. However, the study was limited in two key respects. Firstly, it relied on ‘same-model’ validation. When the same simulation framework is used for both emulator training and the generation of the fiducial ‘observed’ data, the results may be artificially precise and fail to account for the systematic modeling uncertainties. Second, the study shares a common vulnerability in its error treatment, utilizing sample variance under the Gaussian assumption for a signal that is known to be highly non-Gaussian. This is self-contradictory and underestimates the true errors (Mondal et al. 2016, 2021). This also yields biased estimates of the inferred parameters (Shaw et al. 2020; Mondal et al. 2022).

* E-mail: krishnaanoop71@gmail.com

In this Letter, we revisit these problems by performing a cross-simulation validation while properly accounting for signal non-Gaussianities in the error budget. Our analysis incorporates a realistic treatment of the SKA-Low error budget, including non-Gaussian cosmic-variance errors and system noise. We use a Bayesian neural network (BNN) emulator trained on the 21cmFAST simulation data to infer the mean neutral hydrogen fraction (\bar{x}_{HI}) from mock observations generated by the ReionYuga simulation. Because astrophysical parameters are model-dependent and carry different physical meanings across different simulation codes, we focus on \bar{x}_{HI} as a direct observable quantity independent of the specific model. We demonstrate that while the bispectrum provides a clear statistical gain, the improvement is not drastic, as previously reported (Tiwari et al. 2022) when more realistic error treatments are applied. Furthermore, we examine the systematic offsets between different simulation approaches, which pose a major challenge for inference. The same has been observed in SKA SDC3b: EoR inference¹, suggesting that future constraints will be limited by modeling accuracy.

Throughout the Letter, we adopt the Planck+WP best-fitting values of cosmological parameters (Planck Collaboration et al. 2020).

2 SIMULATING THE FIDUCIAL MODEL

We generate the ‘true’ or fiducial observations using the semi-numerical code ReionYuga² (Mondal et al. 2017). This mock observation is intentionally different from the training dataset used for the emulator to ensure a rigorous test of cross-code validity. The simulation process follows three steps. First, it employs a particle-mesh (PM) N -body code³ (Mondal et al. 2015) to evolve the dark matter distribution. Second, the collapsed halos, which serve as hosts for the ionizing sources, are identified using a Friends-of-Friends (FoF) halo finder⁴ (Mondal et al. 2016). Finally, the ionizing field is constructed based on the set excursion formalism (Furlanetto et al. 2004).

Our fiducial ionization simulation is performed in a cubic comoving volume with a side length of 215.04 Mpc and spatial resolution of 0.56 Mpc. The specific model parameters and simulation setup used here are taken directly from (Mondal et al. 2017). For an exhaustive description of the simulation physics and the parameter values, we refer the reader to that work. We analyze six snapshots at redshifts $z = \{7.0, 8.0, 9.0, 10.0, 11.0, 13.0\}$. At each redshift, we use 50 statistically independent realizations, allowing us to estimate the mean power spectrum and bispectrum, as well as associated cosmic variance errors.

The total uncertainty in our mock measurements is driven by two primary components, system noise (σ_{sys}) and cosmic variance (σ_{CV}). System noise is an instrumental effect that is statistically uncorrelated between modes and dominates the error budget at small spatial scales. Conversely, cosmic variance represents the intrinsic statistical uncertainty arising from the finite cosmological volume accessible to observers, dominating on large scales due to the limited number of independent Fourier modes available (see e.g., Mondal et al. 2015).

Rather than adopting a simplified analytical model for these errors, we use a simulation-based approach to calculate the total noise (cosmic variance plus system noise). System noise for a 128 hour observation with the future SKA-Low is generated following the

interferometric noise methodology detailed in Shaw et al. (2019). We inject independent realizations of this thermal noise directly into the 50 brightness temperature (δT_b) cubes. Subsequently, the total errors in the power spectrum and bispectrum measurements are calculated from these 50 statistically independent realizations of the signal. This ensures that our estimates naturally incorporate the non-Gaussian nature of the 21-cm signal. For further discussion of this error estimation method, the reader is referred to Mondal et al. (2021).

3 SIMULATING THE INFERENCE MODEL

To simulate inference models, we use the publicly available 21cmFAST code (Mesinger et al. 2011). This framework efficiently produces three-dimensional brightness temperature fields by applying first-order perturbation theory for structure formation and an excursion-set formalism to identify ionized regions based on the local collapsed fraction. To maintain consistency, we simulate a box size and spatial resolution identical to those used in our fiducial model.

The ionization process is parameterized mainly using three physically motivated quantities. First, the ionizing efficiency parameter HII_EFF_FACTOR (or ζ_0), which represents a combination of several factors, e.g., the star formation efficiency, the number of ionizing photons produced per baryon, and the escape fraction of these photons. Second, R_BUBBLE_MAX defines the maximum mean free path of ionizing photons. Third, ION_Tvir_MIN represents the minimum virial temperature required for a halo to star-forming galaxies (Greig & Mesinger 2015). We generate δT_b snapshots at the same six redshifts used for the fiducial model.

A dataset was constructed using Latin hypercube sampling with 1000 points to ensure efficient coverage of the parameter space. The parameter ranges span $\text{HII_EFF} \in [10, 100]$, $\text{R_BUBBLE_MAX} \in [5, 30]$ and $\log_{10}(\text{ION_Tvir_MIN}/\text{K}) \in [4.0, 5.7]$. From each simulation box, we extract the \bar{x}_{HI} and compute summary statistics, i.e., the power spectrum and the bispectrum. In our emulator, discussed in Section 5, these \bar{x}_{HI} serve as input while the summary statistics are the output.

4 SUMMARY STATISTICS

We characterize the 21-cm signal using two summary statistics: the spherically averaged power spectrum (SAPS) and the spherically averaged bispectrum (SABS). Together, these statistics capture both the Gaussian and the higher-order non-Gaussian information content of the brightness temperature field.

The power spectrum quantifies the spatial fluctuations in δT_b at various length scales. Assuming statistical homogeneity, it is defined as (Mondal et al. 2015)

$$P(\mathbf{k}) = V^{-1} \langle \Delta_b(\mathbf{k}) \Delta_b(-\mathbf{k}) \rangle, \quad (1)$$

where $\Delta_b(\mathbf{k})$ is the Fourier transform of δT_b and V is the comoving volume under consideration. The dimensionless power spectrum, $\Delta^2(k) = k^3 P(k) / 2\pi^2$, for the fiducial model at $z = 8$ is shown in the left panel of Fig. 1. The power spectrum increases monotonically toward smaller scales (larger k), characteristic of the mid-reionization regime, where the growth of ionized bubbles and the density contrast on these scales enhance the power (Bharadwaj & Ali 2004; Mondal et al. 2017). On larger scales (small k), fluctuations are relatively suppressed because the brightness temperature distribution is more

¹ <https://sdc3.skao.int/challenges/inference>

² <https://github.com/rajeshmondal18/ReionYuga>

³ <https://github.com/rajeshmondal18/N-body>

⁴ <https://github.com/rajeshmondal18/FoF-Halo-finder>

uniform. In the figure, we also show the $1\text{-}\sigma$ errors ($\sigma_{\text{sys}} + \sigma_{\text{CV}}$) on the power spectrum calculated from the ensemble of 50 statistically independent realizations of the fiducial signal.

The bispectrum is the lowest-order statistic that can capture the non-Gaussianity in a signal. It records the correlation between three Fourier modes and is defined as (Bharadwaj & Pandey 2005; Mondal et al. 2021)

$$B(\mathbf{k}_1, \mathbf{k}_2, \mathbf{k}_3) = V^{-1} \delta_{\mathbf{k}_1 + \mathbf{k}_2 + \mathbf{k}_3}^K \langle \Delta_b(\mathbf{k}_1) \Delta_b(\mathbf{k}_2) \Delta_b(\mathbf{k}_3) \rangle. \quad (2)$$

Here, the Kronecker delta function δ^K imposes the triangular closure condition $\mathbf{k}_1 + \mathbf{k}_2 + \mathbf{k}_3 = 0$. We compute the SABS for all unique closed triangle configurations using the DviSUKTA code⁵ (Mondal et al. 2021), employing the $(k_1, n, \cos \theta)$ parametrization from Bharadwaj et al. (2020). Here, $k_1 = |\mathbf{k}_1|$ is the longest side, $n = k_2/k_1$ ($\in (0, 1]$) is the side ratio, and $\cos \theta = -\hat{\mathbf{k}}_1 \cdot \hat{\mathbf{k}}_2$ ($\in [0.5, 1]$) defines the shape of the triangle. In Fig. 1, we also show the dimensionless SABS, $\Delta^3(k_1, n, \cos \theta)$ for the fiducial model at $z = 8$ for the squeezed limit ($n \rightarrow 1$, $\cos \theta \rightarrow 1$, so $k_3 \rightarrow 0$), equilateral triangles ($n \rightarrow 1$, $\cos \theta \rightarrow 0.5$, so $k_1 \approx k_2 \approx k_3$), and linear (collinear) triangles ($\cos \theta \rightarrow 1$ fixed, n varying). The squeezed-limit bispectrum typically shows the largest amplitude, reflecting the strong coupling between large-scale modulation and small-scale ionization structures (Majumdar et al. 2018). Other shapes capture important EoR physics because different triangle configurations probe different mode couplings and hence distinct aspects of the signal (Mondal et al. 2021). The $1\text{-}\sigma$ errors ($\sigma_{\text{sys}} + \sigma_{\text{CV}}$) on the SABS were calculated from the fiducial signal ensemble. In our analysis, we retain only configurations with $\text{SNR} > 1$.

5 EMULATORS

To facilitate rapid exploration of the parameter space, we construct a Bayesian neural network (BNN) emulator for both the power spectrum and bispectrum at $z = \{7, 8, 9, 10, 11, 13\}$. For the power spectrum, we train individual BNNs at each redshift to map $\bar{x}_{\text{H I}} \rightarrow P(k)$ onto a fixed k -grid. For the bispectrum, we emulate $\bar{x}_{\text{H I}} \rightarrow B(k_1, n, \cos \theta)$ on a discrete grid of triangular configurations. Emulating the bispectrum is therefore more challenging due to its high dimensionality. Both emulators are trained and evaluated on a suite of 1,000 simulated models, randomly partitioned into an 800-sample training set and a 200-sample testing set.

We used the Keras package in TensorFlow (Abadi et al. 2015; Chollet et al. 2015) to construct the network. Our architecture consists of three hidden layers with 64, 128, and 64 neurons, respectively, utilizing Rectified Linear Unit (ReLU) activations. To prevent overfitting and ensure approximate Bayesian inference, we incorporate Monte Carlo (MC) dropout (Gal & Ghahramani 2016) with a preset dropout rate ($p = 0.10$). This allows us to obtain the epistemic uncertainty (σ_{emu}) associated with the emulators. This uncertainty is propagated into the likelihood via additional emulator variance terms. The coefficient of determination (R^2) for the power spectrum emulator is 0.98, indicating that 98% of the variance in the training data is explained. The bispectrum emulator achieves $R^2 = 0.71$, substantially lower than the power spectrum emulator, reflecting the inherently more complex and nonlinear nature of the $\bar{x}_{\text{H I}} \rightarrow B(k_1, n, \cos \theta)$ mapping compared to $\bar{x}_{\text{H I}} \rightarrow P(k)$.

6 INFERENCE FRAMEWORK

We perform Bayesian parameter inference using the emcee ensemble sampler (Foreman-Mackey et al. 2013). Our analysis compares two cases: (i) an inference based exclusively on power spectrum, and (ii) a joint analysis combining $P(k)$ and $B(k_1, n, \cos \theta)$. To ensure that $\bar{x}_{\text{H I}} \in [0, 1]$, we operate in logit-transformed space, $u_z = \text{logit}[\bar{x}_{\text{H I}}(z)]$.

A central challenge in cross-simulation validation is the inherent systematic bias between different modeling frameworks. To address this, we adopt an input calibration scheme motivated by the Bayesian calibration formalism for computer models developed by (Kennedy & O’Hagan 2002) and extended by (Higdon et al. 2008). The emulator is trained on a globally calibrated input, $\bar{x}_{\text{H I}}^{\text{emu}} = \sigma(u_z + \delta_{\text{global}})$, where σ is the sigmoid function and δ_{global} is the input deformation factor that accounts for the systematic bias in the emulator. Additionally, we introduce a global amplitude parameter, A , to capture multiplicative calibration offsets. We apply uniform priors for nuisance parameters with strict limits $\log A \in [-5, 5]$ and $\delta_{\text{global}} \in [-2, 2]$ in the logit space to ensure the parameter values remain meaningful. By marginalizing over the nuisance parameters A and δ , we obtain meaningful constraints on $\bar{x}_{\text{H I}}$ while mitigating the effects of cross-simulation mismatches. This strategy will be vital for future SKA observations (see e.g., SKA SDC3b: EoR inference⁶).

For the power spectrum, the likelihood is defined as:

$$\mathcal{L}_{\text{P}} \propto \exp \left[-\frac{1}{2} \left(\Delta_{\text{P}}^T \mathbf{C}_{\text{P}}^{-1} \Delta_{\text{P}} \right) \right], \quad (3)$$

where the residual vector $\Delta_{\text{P}} = P_{\text{obs}}(k) - A \cdot P_{\text{emu}}(k | \bar{x}_{\text{H I}}^{\text{emu}})$. The covariance matrix \mathbf{C}_{P} incorporates cosmic variance, system noise, epistemic uncertainty and a conservative 20% modeling error σ_{model} .

For the bispectrum, we employ a likelihood formalism similar to equation 3. However, because computing the full covariance for hundreds of triangle configurations is computationally expensive, we adopt a diagonal likelihood approximation. We replace the full covariance matrix with the diagonal variance $\sigma_B^2(z, \alpha)$, where $\alpha \equiv (k_1, n, \cos \theta)$. This approach captures the dominant contributions to the likelihood and is commonly adopted in previous bispectrum analyses (Mondal et al. 2015; Shaw et al. 2020).

For the combined analysis, we employ an informative multivariate Gaussian prior on $\bar{x}_{\text{H I}}(z)$, obtained from the power spectrum MCMC posterior, acknowledging that any bispectrum measurement would be determined in combination with existing power spectrum constraints. The MCMC sampling is performed with $N_{\text{walkers}} = 64$, running for up to 30,000 steps, where adaptive convergence is implemented.

7 RESULTS

The resulting posteriors are shown in Fig. 2. The results for $P(k)$ alone are shown in blue, and for $B(k_1, n, \cos \theta)$ with informative prior from $P(k)$ are shown in orange. The joint analysis yields constraints on $\bar{x}_{\text{H I}}$ that are roughly 1.4 times more stringent than the power spectrum results. Notably, the degree of improvement does not scale linearly with the number of triangle configurations. For instance, constraints at $z = 9$ and $z = 10$ show better fractional gains than at $z = 8$, despite having fewer triangle configurations ($\text{SNR} > 1$). This reflects the fact that the bispectrum provides non-redundant information that is unique to specific stages of reionization.

⁵ <https://github.com/rajeshmondal18/DviSukta>

⁶ <https://sdc3.skao.int/challenges/inference>

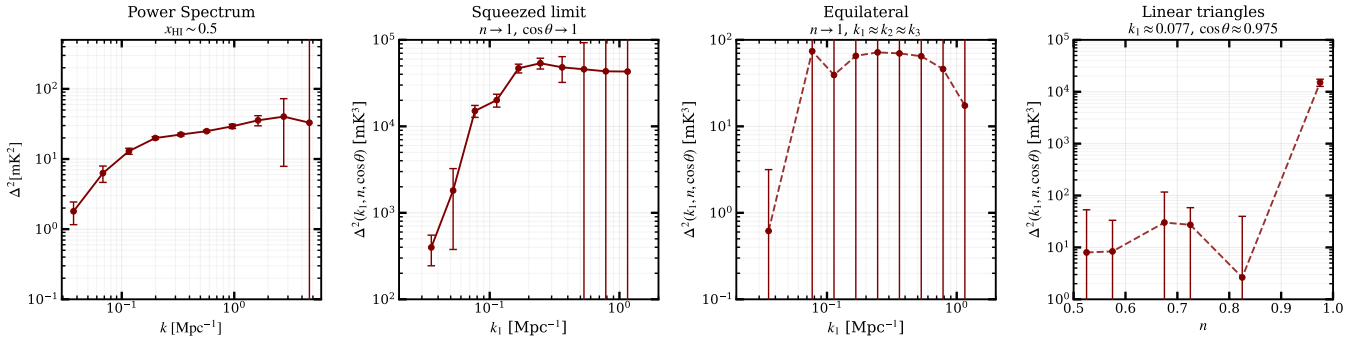


Figure 1. Summary statistics of the fiducial 21-cm signal at $z = 8$. The panels display (from left to right): the SAPS, followed by the SABS in the squeezed limit, equilateral configuration, and linear triangles.

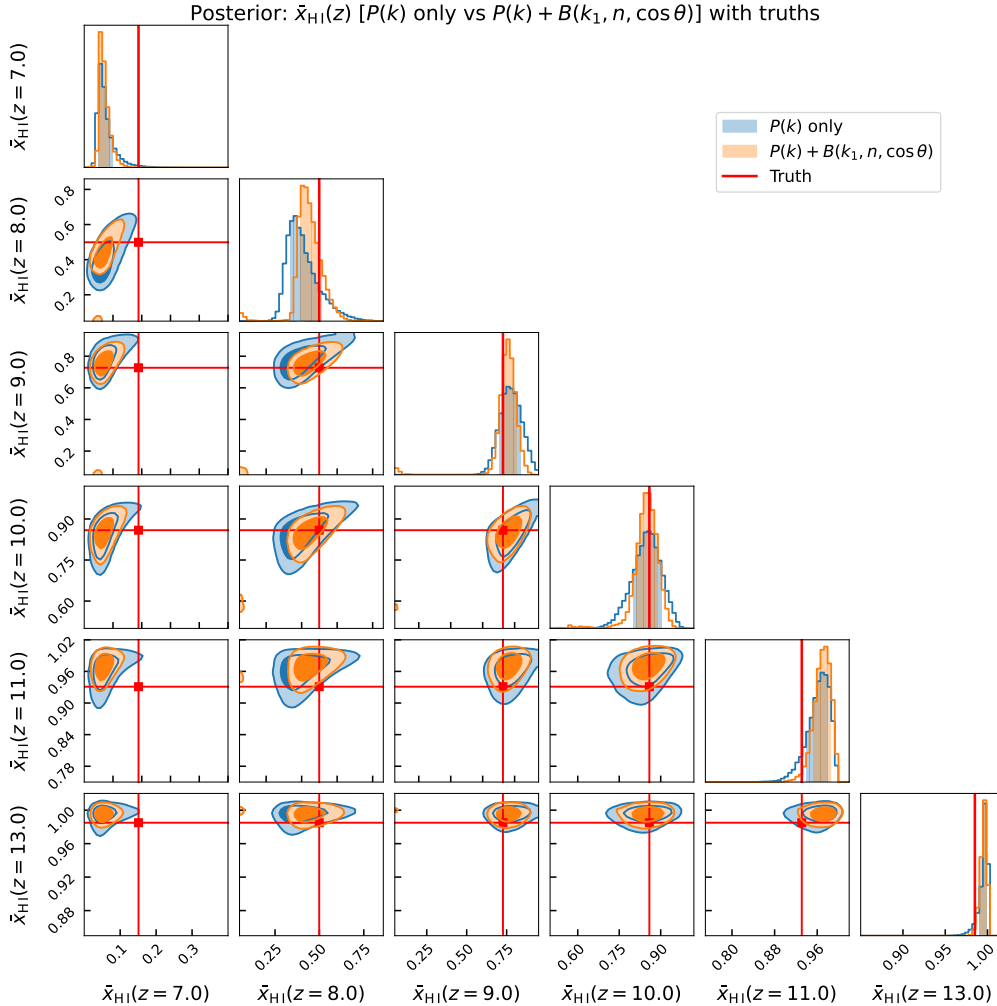


Figure 2. The posterior distribution (1D and 2D) corresponding to \bar{x}_{HI} at $z = \{7, 8, 9, 10, 11, 13\}$ for power spectrum-only (blue) and joint power spectrum-bispectrum (orange) analysis. The shaded region represents 1σ uncertainties.

However, even with the inclusion of nuisance parameters, a systematic offset remains visible between the ‘true’ and the inferred values. While A and δ partially mitigate discrepancies in cross-simulation validation, they cannot fully capture the redshift-dependent physical differences between ReionYuga and 21cmFAST. This persistent bias, consistent with the findings of Zahn et al. (2011); Majumdar

et al. (2014), suggests that future constraints may be more limited by the algorithmic assumptions of our simulation frameworks.

8 CONCLUSION & DISCUSSION

We have performed a stringent cross-simulation validation of 21-cm inference during the EoR, training a BNN on 21cmFAST simulation and applying it to a ‘true’ model generated by the independent ReionYuga framework. This setup ensures that the interpolation capability of emulators is tested against an independent and potentially more realistic model of the universe. Our analysis jointly utilizes the power spectrum and the bispectrum to constrain \bar{x}_{HI} at six different redshifts $z = \{7, 8, 9, 10, 11, 13\}$. The error budget rigorously incorporates cosmic variance, system noise, \bar{x}_{HI} -dependent epistemic uncertainty, and modelling error. Notably, the cosmic variance and system noise are accounted for directly at the level of the 21-cm brightness-temperature cubes. Thereafter, all statistics are computed from 50 statistically independent realizations of the signal. This treatment is more robust than the Gaussian approximations common in previous studies, which underestimate uncertainties by 20–50% and yield biased estimates of the inferred parameters (Trott et al. 2016; Mondal et al. 2016; Greig & Mesinger 2017; Shaw et al. 2020; Tiwari et al. 2022).

Rather than adopting model-dependent astrophysical parameters, we infer a direct observable \bar{x}_{HI} . Our results reveal that incorporating the bispectrum yields constraints ~ 1.4 times more stringent than the power spectrum alone, with the most significant gains occurring during mid-reionization. This is consistent with theoretical expectations that higher-order statistics encode additional information inaccessible to the power spectrum alone (Watkinson et al. 2017; Majumdar et al. 2018; Mondal et al. 2020; Kamran et al. 2021). In addition, we find that the information content does not scale linearly with the addition of the bispectrum of different configurations. Instead, a small number of effective configurations, such as the squeezed limit, capture the bulk non-Gaussian information in the signal.

Despite these statistical improvements, our study reveals a persistent systematic bias between inference and the true model. This reflects the highly model-dependent nature of \bar{x}_{HI} when derived from specific simulation frameworks. The bias remains evident in both the power spectrum and joint analysis, becoming even more evident when the bispectrum tightens the statistical bounds. A similar phenomenon is also observed in the SKA SDC3b. While the global nuisance parameters A and δ partially mitigated these biases, they are still inadequate to capture the redshift-dependent offset. This indicates that the discrepancy does not arise from simple normalization or calibration differences but instead reflects fundamental structural differences in how reionization physics is implemented across simulation frameworks.

A key implication for future SKA observations is that reports of sub-percent uncertainty on \bar{x}_{HI} may be overconfident if they rely on ‘same-code’ validation. Our cross-simulation results highlight that systematic modeling uncertainty remains the dominant bottleneck. Accurate inference will therefore require statistical frameworks that explicitly account for these model-dependent effects.

ACKNOWLEDGEMENTS

RM is supported by the NITC FRG Seed Grant (NITC/PRJ/PHY/2024-25/FRG/12).

DATA AVAILABILITY

The data underlying this article will be shared on a reasonable request to the corresponding author.

REFERENCES

- Abadi M., et al., 2015, TensorFlow: Large-Scale Machine Learning on Heterogeneous Systems, <https://www.tensorflow.org/>
- Becker R. H., et al., 2001, *The Astronomical Journal*, 122, 2850
- Bharadwaj S., Ali S. S., 2004, *MNRAS*, 352, 142
- Bharadwaj S., Pandey S. K., 2005, *MNRAS*, 358, 968
- Bharadwaj S., Mazumdar A., Sarkar D., 2020, *Monthly Notices of the Royal Astronomical Society*, 493, 594
- Chollet F., et al., 2015, Keras, <https://keras.io>
- DeBoer D. R., et al., 2017, *PASP*, 129, 045001
- Foreman-Mackey D., et al., 2013, emcee: The MCMC Hammer, *Astrophysics Source Code Library*, record ascl:1303.002 (ascl:1303.002)
- Furlanetto S. R., Zaldarriaga M., Hernquist L., 2004, *ApJ*, 613, 16
- Furlanetto S. R., Oh S. P., Briggs F. H., 2006, *Phys. Rep.*, 433, 181
- Gal Y., Ghahramani Z., 2016, in Balcan M. F., Weinberger K. Q., eds, *Proceedings of Machine Learning Research* Vol. 48, *Proceedings of The 33rd International Conference on Machine Learning*. PMLR, New York, New York, USA, pp 1050–1059, <https://proceedings.mlr.press/v48/gal16.html>
- Greig B., Mesinger A., 2015, *MNRAS*, 449, 4246
- Greig B., Mesinger A., 2017, *MNRAS*, 472, 2651
- Higdon D., Gattiker J., Williams B., Rightley M., 2008, *Journal of the American Statistical Association*, 103, 570
- Iliev I. T., Mellema G., Pen U.-L., Merz H., Shapiro P. R., Alvarez M. A., 2006, *MNRAS*, 369, 1625
- Kamran M., Ghara R., Majumdar S., Mondal R., Mellema G., Bharadwaj S., Pritchard J. R., Iliev I. T., 2021, *MNRAS*, 502, 3800
- Kennedy M. C., O’Hagan A., 2002, *Journal of the Royal Statistical Society Series B: Statistical Methodology*, 63, 425
- Majumdar S., Mellema G., Datta K. K., Jensen H., Choudhury T. R., Bharadwaj S., Friedrich M. M., 2014, *MNRAS*, 443, 2843
- Majumdar S., Pritchard J. R., Mondal R., Watkinson C. A., Bharadwaj S., Mellema G., 2018, *MNRAS*, 476, 4007
- Mesinger A., Furlanetto S., Cen R., 2011, *MNRAS*, 411, 955
- Mondal R., Bharadwaj S., Majumdar S., Bera A., Acharyya A., 2015, *MNRAS*, 449, L41
- Mondal R., Bharadwaj S., Majumdar S., 2016, *MNRAS*, 456, 1936
- Mondal R., Bharadwaj S., Majumdar S., 2017, *MNRAS*, 464, 2992
- Mondal R., Shaw A. K., Iliev I. T., Bharadwaj S., Datta K. K., Majumdar S., Sarkar A. K., Dixon K. L., 2020, *MNRAS*, 494, 4043
- Mondal R., Mellema G., Shaw A. K., Kamran M., Majumdar S., 2021, *MNRAS*, 508, 3848
- Mondal R., Mellema G., Murray S. G., Greig B., 2022, *Monthly Notices of the Royal Astronomical Society: Letters*, 514, L31
- Morales M. F., Wyithe J. S. B., 2010, *ARA&A*, 48, 127
- Planck Collaboration et al., 2020, *A&A*, 641, A6
- Pritchard J. R., Loeb A., 2012, *Reports on Progress in Physics*, 75, 086901
- Shaw A. K., Bharadwaj S., Mondal R., 2019, *MNRAS*, 487, 4951
- Shaw A. K., Bharadwaj S., Mondal R., 2020, *Monthly Notices of the Royal Astronomical Society*, 498, 1480
- Tingay S. J., et al., 2013, *Publ. Astron. Soc. Australia*, 30, e007
- Tiwari H., Shaw A. K., Majumdar S., Kamran M., Choudhury M., 2022, *Journal of Cosmology and Astroparticle Physics*, 2022, 045
- Trott C. M., et al., 2016, *ApJ*, 818, 139
- Watkinson C. A., Majumdar S., Pritchard J. R., Mondal R., 2017, *MNRAS*, 472, 2436
- Zahn O., Mesinger A., McQuinn M., Trac H., Cen R., Hernquist L. E., 2011, *MNRAS*, 414, 727
- van Haarlem M. P., et al., 2013, *A&A*, 556, A2

This paper has been typeset from a \LaTeX file prepared by the author.